

NUMERICAL SIMULATION OF INDOOR AIR DISTRIBUTION AND WALL HEAT STORAGE UNDER ACCIDENT CONDITIONS IN A MAIN CONTROL ROOM

by

Huikang CAI, Shuaijie SHA, Tai XU, Yannan LI, and Hanzhong TAO*

School of Energy Science and Engineering, Nanjing Tech University, Jiangsu, China

Original scientific paper
<https://doi.org/10.2298/TSCI240119100C>

The main control room serves as a refuge for staff in a nuclear power plant in the event of an accident. To determine whether the control room can meet habitability requirements under accident conditions, this study utilized CFD methods to establish a habitability model of the main control room under such conditions. The changing trends of temperature and velocity near personnel were analyzed. The numerical results indicate that the building envelope significantly contributes to reducing the indoor temperature. The average wall temperature measured at 72 hours was 27 °C, with an average temperature increase of 4 °C. The highest average ambient temperature in the main control room occurred at 24 hours. At this time, the indoor ambient temperature reached approximately 34.62 °C, with a temperature increase of 11.62 °C, while the wind speed near the personnel remained below 0.2 m/s, meeting habitability requirements for personnel under extreme conditions.

Key words: *CFD simulation, habitability of main control room, heat storage of envelope, nuclear power plant*

Introduction

As an important form of energy, nuclear energy has the characteristics of safety, cleanliness and economy, and can be used on a large-scale [1]. However, the Fukushima nuclear accident [2] in Japan has made people worried about the safety of nuclear power. This nuclear crisis was the largest nuclear accident after the Chernobyl nuclear disaster on April 26, 1986 [3], resulting in serious casualties of nuclear power plant (NPP) staff [4]. Since then, people have paid increased attention the safety of nuclear power.

To reduce the number of casualties during accidents, it is necessary to establish a safe and healthy environment for the staff. This temporary shelter can be the main control room (MCR), which is the main control center of the whole NPP. In the event of a nuclear accident, the MCR protects the occupants from the harmful effects of radioactive substances, explosive substances and toxic gases with high radiation levels [5, 6] due to the isolated air purification and ventilation system [7]. The shutdown of the NPP is a complex process, therefore, it leads to a long-term, usually 72 hours occupancy period in the MCR [8]. The indoor air temperature will increase as a result of the internal heat loads generated by the human bodies and technical equipment [9]. If the air temperature in the MCR exceed the upper limit of human heat tolerance, 35 °C wet-bulb temperature [10, 11], it will pose a danger to the safety of employees.

* Corresponding author, e-mail: taohanzhong@njtech.edu.cn

To ensure and maintain the acceptable thermal environmental conditions for indoor personnel to survive, measures must be taken in the MCR to maintain the acceptable indoor thermal condition [12].

Room temperature range has a significant impact on indoor environmental quality. Under normal operating conditions, the allowable temperature range can be maintained using the central air conditioning system of the MCR. However, if an accident occurs, the air conditioning system cannot operate in the event of power failure. To solve this problem, the AP1000 NPP's passive safety system has been developed to ensure the fundamental functions using only natural effects, *e.g.* by compressed air expansion [13]. Some research conducted on passive refrigeration in the MCR of NPP. Li *et al.* [8] studied the use of isentropic expansion of compressed air for refrigeration, and the results show that this method can meet the requirements of occupancy in the MCR. Jia *et al.* [14] studied the ice storage bin of the coal mine shelter, tested the effective cooling time of the system, and provided help for the temperature control of the shelter. Wang *et al.* [15] proposed a new compressed air refrigeration system, which reduces the operation cost of the system. Siddiqui *et al.* [16] conducted an economic analysis of the hybrid storage absorption refrigeration cycle system.

In addition, the cold storage technology of concrete structures [17] can significantly reduce the indoor temperature of the MCR. The internal heat gain result difference between the walls and the room air temperature. Due to the heat transfer through the walls and the thermal storage reinforced concrete structures. The indoor air temperature remains within the acceptable limits. are used to store heat, to discharge the indoor heat dissipation and maintain the indoor temperature. Huang *et al.* [18] studied the dynamic thermal process of the concrete ceiling with fins in the MCR, and maintained the thermal habitability of the MCR through the ceiling made of concrete. Al-Rukaibawi *et al.* [19] numerically studied the influence of envelope structure on overheating risk in summer, and analyzed the overheating problem and thermal comfort of four envelope structure. Gollapudi *et al.* [20] numerically analyzed the heat transfer performance of envelope with horizontal fins.

In summary, indoor air temperature is an important reference factor. For NPP, before implementing various passive cooling facilities in the design and lay-out of the MCR that operate naturally without relying on electricity, it is necessary to investigate whether habitability indoor can be maintained solely through its own enclosed structure for up to 72 hours. However, there is little research on this aspect at present. Therefore, this study aims to fill this gap by establishing a finite volume CFD program. Through the CFD simulation technology, we can obtain detailed distributions of the indoor thermal environment and provide a reference for future optimization. Based on a small NPP, the heat storage of the MCR wall envelope is considered, and a ventilation system for precooling air supply is applied in this study. The system primarily uses the compressed air tanks to spray low temperature fresh air and mix it with indoor return air to reduce the supply air temperature to a certain extent. Meanwhile, RNG $k-\varepsilon$ turbulence model and models for equipment with certain heating power and human body heat generation are established. Finally, the indoor air-flow field and temperature field of the MCR under accident conditions are analyzed.

Numerical simulation

Physical models

A 3-D model of the same size ($17.55 \text{ m} \times 14.15 \text{ m} \times 4.1 \text{ m}$) as the interior of the MCR was established. In this study, the heat storage effect of the upper and lower walls was not considered, as they are exposed to high temperature environments. Instead, the surfaces of the

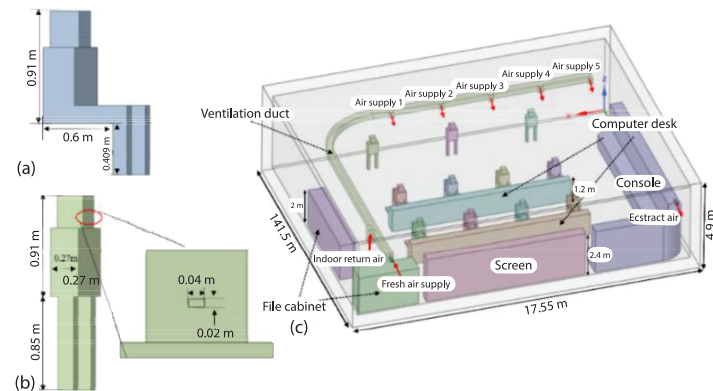


Figure 1. (a) People in sitting position; (b) people in standing position, and (c) 3-D model of the MCR

upper and lower walls were treated as adiabatic walls. The wall surrounding the MCR is shared with other rooms on the same floor, which means that the temperature of the wall on the MCR side can be affected by heat dissipation from other rooms. To accurately capture this effect, only half thickness of the wall was used in the model, with a thickness of 0.4 m. Figure 1 shows the established 3-D model. In this model, the MCR consists of walls, equipment, ventilation ducts and personnel. The equipment includes console, screen, and computer desks. The human body model was established based on *Chinese Adult Human Body Dimensions*, as shown in figs. 1(a) and 1(b). Human breathing is considered in this paper, and the breathing area is $0.04 \text{ m} \times 0.02 \text{ m}$ rectangle. In this model, 11 people were divided into three rows, the first two rows are in a sitting position and the 3rd row is in a standing position.

The MCR is preset with fresh air to ensure the survival of personnel for 72 hours, which is stored in the compressed air tank. When an accident occurred, fresh air was ejected from the compressed air tank into the ventilation ducts and mixed with the indoor return air to reduce the temperature of the supply air. There are five air supply outlets in the MCR. The center height of the air supply outlet is 3 m, and the air supply direction is at an angle of 0° with the horizontal direction. Considering the penetration of indoor air, an outlet is set at the upper end of the side wall.

Equipment and human models are shown in fig. 1(c), in which the heating area of the large screen is 44.8 m^2 , the heating area of the console is 82.41 m^2 , and the heating area of the computer desk is 71.28 m^2 . The cross-sectional area of the fresh air inlet is 0.01 m^2 , the cross-sectional area of the supply air is 0.064 m^2 , and the cross-sectional area of the return air is 0.1024 m^2 . To reduce the grid and save computing resources, the surface without thickness was used to build equipment and personnel.

Monitoring planes and lines

For further research, monitoring planes and monitoring lines are set in the MCR to obtain the changes of indoor flow pattern and temperature field. The height of people sitting indoors is about 1.3 m, and the height of people standing is about 1.8 m. To study the indoor habitability and capture the flow field and temperature field at the neck and ankle of personnel, monitoring planes P1-P3 and monitoring lines L1-L12 are set in the occupied area of personnel. The monitoring plans P1 ($y = 1.6 \text{ m}$), P2 ($y = 5.3 \text{ m}$), and P3 ($y = 8.3 \text{ m}$), respectively pass through three rows of people, and the monitoring lines L1-L12 is distributed in the habitable

area by people, as shown in figs. 2(a) and 2(b). To study the flow field and thermal conditions in the habitable area under different personnel distributions, the habitable area with a height of 0-2.2 m is drawn, as shown in fig. 2(c).

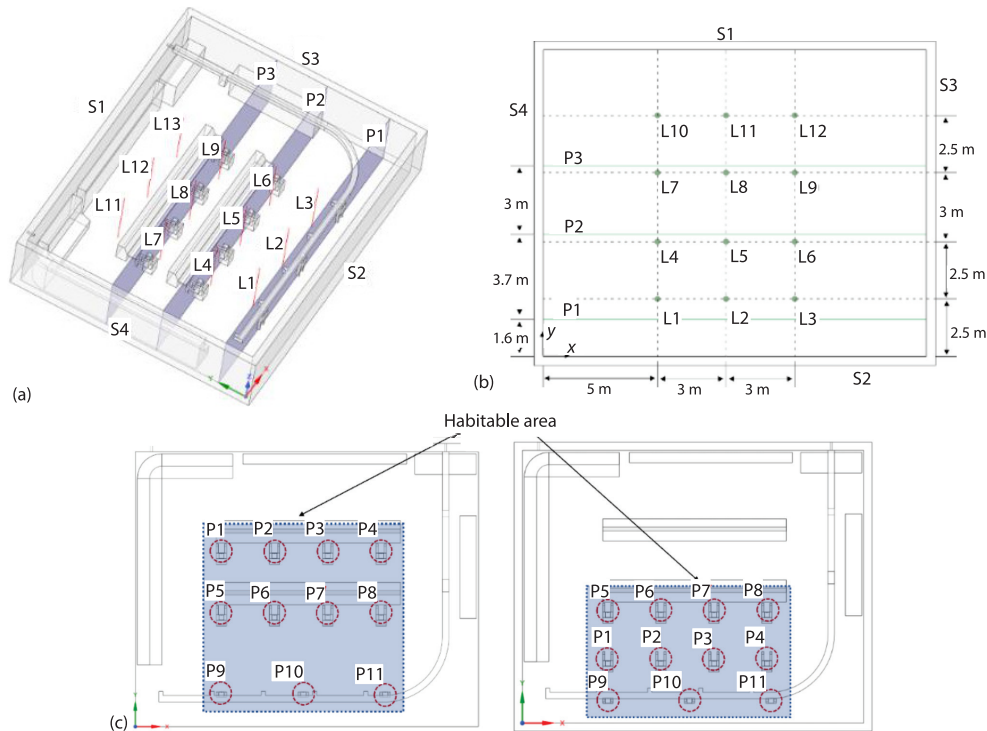


Figure 2. Schematic view of monitoring plans and lines; (a) 3-D schematic view, (b) details of monitoring plans and lines, and (c) location of the habitable area of the MCR in Cases 1 and 3

Boundary conditions

To evaluate the habitability of the MCR under accident conditions, this paper adopts the numerical simulation method. Table 1 shows the heat dissipation of each heat source in MCR under accident conditions. According to the data in tab. 1, under accident conditions, the ventilation system is closed or isolated to prevent pollutants from entering MCR. The equipment remains in operation for 24 hours to perform the safe shutdown task and generates heat. The total heat dissipation in MCR at this stage is 12 kW. After 24 hours, the equipment shuts down after performing the safe shutdown task. During this period, the total heat dissipation of MCR is 1 kW.

Heat gain refers to the additional heat absorbed by a building or system, resulting in an increase in indoor temperature. Heat gain is an important consideration in architectural engineering and HVAC design because it affects indoor temperatures and the load on HVAC systems. In this paper, indoor heat gain includes equipment heat dissipation and metabolic heat production from indoor personnel. When a person sits quietly in the MCR, the metabolic rate of the human body is 1 met and is equal to 91 W total heat gain. The equipment operates normally in the first 24 hours, so the surface heat flow is defined as 66.96 W/m², 72.81 W/m², and

Table 1. Heat dissipation of heat source in MCR

	Heat source area [m ²]	Heat dissipation [kW]	
		0-24 hours	24-72 hours
Screen	44.8	3	0
People	24.54	1	1
Console	82.41	6	0
Computer desk	721.28	2	0
Total heat dissipation		12	1

28.06 W/m² for the screen, console, and computer desk, respectively. After 24 hours, the equipment stopped running and the surface heat flow changed to 0 W/m². Meanwhile, the non-slip condition was imposed on all solid walls.

The velocity inlet boundary condition is set at the fresh air supply. The temperature of fresh air provided is 15 °C, and the air-flow is 113 m³ per hour. The turbulence intensity and hydraulic diameter of the inlet are calculated:

$$d = \frac{4A}{S} \quad (1)$$

$$\text{Re} = \frac{\nu d}{\mu} \quad (2)$$

$$I = 0.16\text{Re}^{-0.125} \quad (3)$$

Pressure outlets serve as the boundary conditions for the outlet, while indoor return air and the five air supply outlets are designated as fan boundaries. Fan boundaries require specification of pressure drop and direction determine fluid-flow and orientation. Specifically, the pressure jump for indoor return air is set to 17 Pa, and for the five air supply outlets, the pressure jumps are individually configured as 7.5 Pa, 6.5 Pa, 6 Pa, 4.5 Pa, and 3.5 Pa. Their average direction aligns with the positive y-axis. The indoor return air-flow rate is set at 1020 m³ per hour, with the zone-average direction aligned to the positive z-axis, as illustrated in fig. 1(c). The indoor inlet air velocity is 3.14 m/s, and the temperature is maintained at 288 K.

Most of the enclosure structures of the MCR and the control equipment room are composed of reinforced concrete, and the proportion of glass windows in the MCR enclosure structure is small. For the convenience of calculation, they are simplified to reinforced concrete. Non-heat-source objects such as chairs and filing cabinets are set as wood, and the physical parameters of the human body and water are approximated. The physical parameters of each material are shown in tab. 2.

Table 2. Material properties

	Density [kgm ⁻³]	Specific heat capacity [Jkg ⁻¹ K ⁻¹]	Thermal conductivity [Wm ⁻¹ K ⁻¹]
Wall	2650	960	1.74
Chair and file cabinet	700	2310	0.17
People	1048	4200	0.43

Case description

The air domain of the MCR is 16.75 m long, 13.35 m wide and 4.1 m high. The actual thickness of the wall is 0.8 m. Due to the high temperature environment outside of the MCR, the theoretical effective thermal storage thickness of the wall is 0.4 m. The impact of walls, equipment, and personnel on the thermal environment of the MCR are analyzed by using different cases. Case1 is the actual working condition, and in the actual situation, the upper and lower floors of the MCR are in high temperature environment, so heat storage of ceiling and floor are not considered. Case 2 is the ideal working condition, that is, the heat storage of ceiling and floor is considered. To study the impact of personnel position on the thermal environment of the MCR, Case 3 moves the first rows of personnel away the equipment based on Case 1.

Numerical details and grid independence

The model was meshed, and a structured mesh dominated by hexahedron was generated to improve the mesh quality. Grid encryption was carried out for the entrance, exit, human body, and equipment departments to ensure the accuracy of the calculation results. The main advantage of structured grid was that each cell has adjacent nodes. Therefore, compared with tetrahedral mesh, it can better calculate the gradient and reduce the number of meshes. The finite volume numerical method was used to simulate the temperature and air-flow distribution in the room, and this method was used for the diffusion and source terms. A gravitational acceleration along the negative direction of the z-axis was set, the pressure was discretized in a body-weighted format, and the energy and momentum were discretized in a second-order upwind format. To analyze the reliability of the obtained data, a convergence criterion was established, which was less than 10^{-4} for convergence variables except energy, and less than 10^{-8} for energy. The time step is 30 seconds.

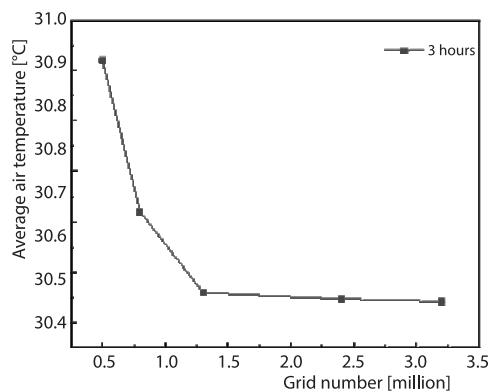


Figure 3. Grid-independence verification

When dividing the grid, different parameters were set to change the size and sparsity of the grid. The grid number of the grid model was divided into 0.5×10^6 , 0.8×10^6 , 1.3×10^6 , 2.4×10^6 and 3.2×10^6 , respectively. Set the same boundary conditions to simulate different grid numbers under no stationary. Using average air temperature parameters to evaluate the influence of grid size on simulation quality. As can be seen from fig. 3, when the number of grids is 1.3×10^6 , the average air temperature began to tend to a fixed value, and the grid became independent. Considering the main computing resources available, the model with 2.4×10^6 grids is selected for calculation.

Results and discussions

Model validation

To verify the reliability of the numerical model for temperature distribution in the MCR, the results obtained from the numerical simulation were compared with the data provided by Palanisamy [21]. Usually, the temperature distribution in the room can be well modelled by CFD. The validation model used is a control room measuring 3 m in length, 6.1 m in width, and 2.4 m in

height. The verification results are shown in the fig. 4, indicating an average error of simulated data is 0.74% and a maximum error of 1.28% for the simulated data. The average error for experimental measurement is 4.13%, with the maximum error of 4.8%. These results demonstrate good agreement between that the numerical simulation results and experimental data.

Thermal storage effect of building envelope

Influence of walls on indoor thermal environment

Firstly, for the case of no wall thermal storage (the ability of wall materials to absorb, store, and release heat), the calculation results show that the indoor air temperature reaches 36.8 °C at 0.5 hours. It can be concluded that this condition cannot meet the livability requirements of the MCR. Then, the dynamic changes of the average MCR air temperature and wall temperature over time were studied for Cases 1 and 2. Figure 5 shows the dynamic changes of the average MCR air temperature over time for the two cases. It can be observed that the air temperature in both Case 1 and Case 2 rapidly increases in the first 0.5 hours. For Case 1, the temperature rises at a rate of 5.35 °C per hour and 0.18 °C per minute in the first 0.5 hours, and significantly slows down to 0.27 °C per hour from 0.5-24 hours, due to the delayed thermal storage effect of the wall. When the NPP experiences a power outage for 24 hours during the accident, the MCR average air temperature reaches its peak, and the results show that the air temperature for Case 1 at this time is 34.62 °C. After the equipment runs for 24 hours to complete the shutdown task and stops running, the average indoor air temperature begins to decrease. From fig. 5, there is a sudden temperature drop process after the equipment stops running, and then the cooling rate gradually decreases and eventually stabilizes. In the sudden drop process, the average air temperature in Case 1 decreases from 34.62 °C at 24 hours to 29.91 °C at 25 hours, with a temperature decrease of 4.71 °C. The average temperature stabilizes at 27.61 °C at 48 hours.

Case 2 is the ideal condition, considering the thermal storage effect of the ceiling and floor based on Case 1. It can be seen from the figure that the trend of the indoor average air temperature with time for Case 2 is like that of Case 1. In the first 0.5 hours of equipment operation, the air temperature also experiences a sudden temperature rise process. The indoor air temperature of MCR rises by 2.65 °C in the first 0.5 hours, with a temperature rise rate of 5.3 °C per hour. From 0.5-24 hours, the temperature rise rate decreases to 0.18 °C per hour. The indoor air temperature reaches its highest point at 24 hours, which is 27.72. After the equipment stops running for one hour, the indoor air temperature decreases by 1.12 °C, and when the equipment

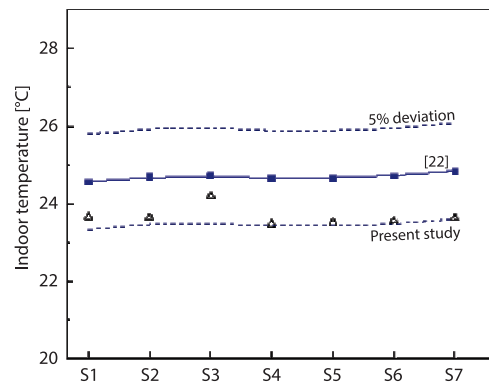


Figure 4. Temperature distribution verification results

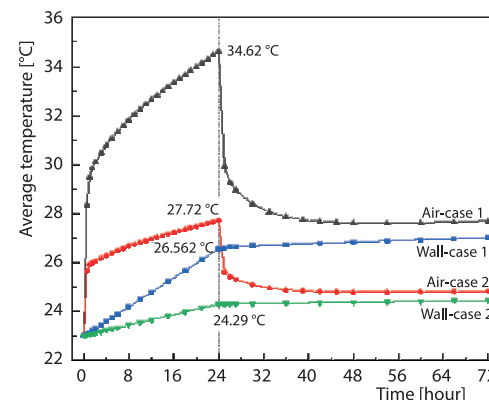


Figure 5. Effect of envelope on indoor air temperature

stops running for 24 hours, the indoor temperature stabilizes at 24.79 °C. The thermal storage of the envelope structure plays a significant role in reducing indoor air temperature and has an important impact on the livability of the MCR.

Unsteady heat transfer in walls

By analyzing the interior of the walls, the overall temperature trend of the walls can be obtained within 0-72 hours, as shown in fig. 5. Figure 5 shows the changes in the overall wall temperature over time for two different operating conditions, Cases 1 and 2. It can be seen that within the first 24 hours, the overall wall temperature increases linearly with time for both cases. After 24 hours, although the equipment stops running, the wall temperature does not decrease as rapidly as the air temperature, because heat transfer within the wall occurs primarily through conduction, whereas the air is influenced by convection and radiation, which makes the wall response slower than the air. Under Case 1, the wall temperature rises from 23-26.56 °C, with a temperature rise of 3.56 °C within 24 hours, at a rate of 0.15 °C per hour. After 24 hours, the overall wall temperature increases slowly due to the cessation of equipment operation, reaching an average temperature of 27 °C by 72 hours, with an average temperature rise of 0.44 °C within 24-72 hours. Under Case 2, the inclusion of ceiling and floor thermal storage enhances the wall's overall thermal storage capacity. In this case, the overall wall temperature rises from 23-24.29 °C, with a temperature rise of 1.29 °C within 24 hours, at a rate of 0.05 °C per hour. After 24 hours, the overall wall temperature tends to stabilize, reaching an average temperature of 24.44 °C by 72 hours, with an average temperature rise of 0.15 °C within 24-72 hours.

To further investigate the temperature field changes inside the wall, Case 1, which is closest to the actual operating conditions, was selected as the research object, and the temperature changes of the four walls were analyzed separately to obtain their individual temperature changes over time.

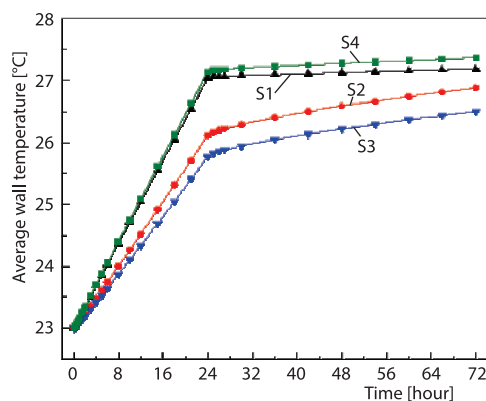


Figure 6. Average temperature variation of the four walls with time

temperature into the walls' internal heat has some impact. From 0-24 hours, the temperature rise rate of the wall in the high heat flux density region is higher than that in the low heat flux density region. The temperature rise rate of wall S4 is 0.173 °C per hour, while wall S3's rise rate is 0.116 °C per hour. After 24 hours, the temperature of walls S1 and S4 is maintained by the residual heat of the equipment, while walls S2 and S3 are far from the heat source, resulting in a relatively low heat flux density near the walls and a lower temperature rise rate of the walls'

Figure 6 shows the variation of the average temperature of the four walls over time, with each wall having a different average temperature. Wall S4 has the largest temperature fluctuation over time, while wall S3 has the smallest temperature fluctuation. This is due to wall S4 being affected by the heat dissipation of the control console and other equipment, resulting in the highest average temperature of the four walls, while wall S1 is most affected by the heat dissipation of the large screen. Compared to walls S1 and S4, there are relatively few devices near-walls S2 and S3, resulting in a lower average temperature of the walls. This indicates that the penetration strength of environmental

average temperature. Within the first 24 hours, wall S3's temperature rise rate is 0.116 °C per hour. The temperature of wall S3 increases by approximately 0.73 °C from 24-72 hours.

Figure 7 displays the time-dependent variation of the surface-averaged temperature at different depths within wall S2. The reference point for this analysis is the interior wall surface in contact with the indoor air, while the outer wall surface serves as the endpoint. The wall is uniformly divided along its thickness, and the surface temperature at each depth is averaged to obtain the temperature variation across the wall's different depths. More specifically, the plot shows the temporal evolution of the surface-averaged temperature at various depths within wall S2. The averaging process is performed by computing the arithmetic mean of the temperature distribution at each depth, obtained by dividing the wall into uniform intervals along its thickness direction. By this means, the plot enables us to visualize how the temperature varies at different depths within the wall over time.

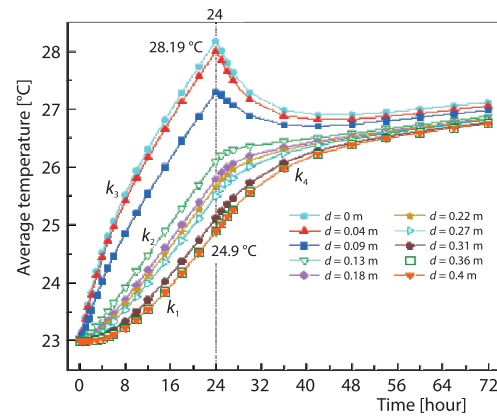


Figure 7. Temperature variation with time at different depths of the wall

The temperature variation trend displayed in the figure highlights the most significant temperature changes over time at a depth of $d = 0$ m. Table 3 reports the fitting function for the temperature change trend observed within 0-24 hours, which follows a monotonic increasing trend described by the equation $T = 0.2146t + 23.457$, and reaches a maximum temperature of 28.19 °C. Within the depth range of 0 m to 0.13 m, the wall is highly sensitive to changes in the ambient temperature, and its heat storage capacity is relatively low. As a result, the wall mainly transmits the heat absorbed by the indoor surface to its interior. The temperature at depths less than 0.13 m reaches its maximum at 24 hours, while the magnitude of the temperature peak decreases with increasing depth. Beyond a depth of 0.13 m, the peak disappears, and the internal thermal conduction of the wall starts to increase as a function of wall depth. Table 3 also presents the time-dependent variation of the wall temperature at a depth of $d = 0.4$ m, which displays a monotonic increasing trend within 0-72 hours. The heating rate during the first 24 hours ($k_1 = 0.077$) is higher than that observed during the subsequent 25-72 hours ($k_4 = 0.026$).

Table 3. Fitting function of temperature at different depths of the wall against time variation

Wall Depth time	$d = 0$	$d = 0.13$	$d = 0.4$
0-24 hours	$T = 0.2146t + 23.457$ $R^2 = 0.97$	$T = 0.1328t + 22.895$ $R^2 = 0.9985$	$T = 0.0767t + 22.796$ $R^2 = 0.9407$
30-72 hours		$T = 0.0123t + 26$ $R^2 = 0.9999$	$T = 0.0257t + 25.028$ $R^2 = 0.9024$

During the period of 0-24 hours, the interior heat flux penetrates the wall to a relatively small distance, resulting in a significant difference in the temperature rise rate of the wall at different depths. The heat transfer from the inner wall is highly affected by the variation in indoor heat flux, but this effect gradually reduces with increasing depth. The fitting model indicates that the increment rate at $d = 0$ m is $k_3 = 0.215$, the temperature rise rate at $d = 0.13$ m is $k_2 = 0.133$, and at $d = 0.4$ m, it is $k_1 = 0.077$.

Indoor temperature and air-flow distribution

Variation of indoor ambient temperature

Based on the numerical simulation results of two cases with and without walls, it was found that walls play a significant role in reducing the temperature in the MCR. To further investigate the impact of personnel positions on the flow and temperature fields within the habitable area under case1 working conditions, an additional standing position for personnel was introduced, as shown in fig. 2(c). The blue area represents the main activity zone of the personnel, with a heat emission rate of 12 kW during the 0-24 hours period, which reduces to 1 kW when the equipment is not in operation during the 24-72 hours period. The average indoor temperature was analyzed accordingly.

Figure 8 presents the temporal variations of indoor air temperature and wall temperature for Cases 1 and 3. The trends of the average wall temperature and ambient temperature are similar in both cases. In Case 1, the green curve – 1, represents the time variation of the average temperature in the MCR from 0-72 hours, and the red curve – 2, shows the time variation of the average temperature of the wall. The temperature exhibits a monotonically increasing trend in the first 24 hours, with a decreasing rate of increase over time. The indoor ambient temperature increased rapidly by 6.4 °C during 0-1 hour, with a high rate of increase of 6.47 °C per hour. After 1 hour, the trend of indoor ambient temperature changed slowly with time, with a rate of increase of 0.22 °C per hour, and the indoor ambient temperature peaked at 34.62 °C at 24 hours. Due to the heat storage lag of the envelope, the indoor ambient temperature rises faster initially and slows down when the envelope starts to absorb heat. After 24 hours, the indoor temperature starts to decrease as the equipment stops running. At 25 hours, the indoor ambient temperature drops by 4.71 °C compared with 24 hours, and the rate of decrease gradually becomes smaller over time until the temperature stabilizes after 48 hours. The rapid rise in indoor ambient temperature during 0-24 hours may have some impact on personnel.

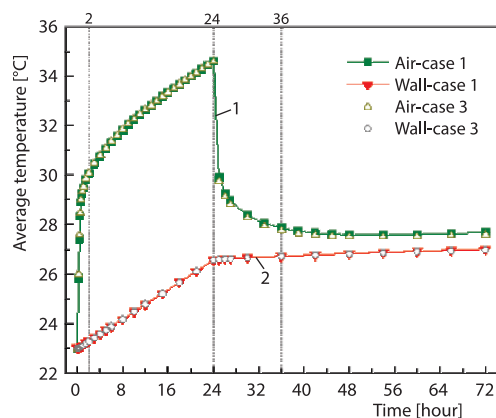


Figure 8. Indoor ambient temperature and wall temperature change with time

Numerical simulations provide valuable insights into the working conditions of the MCR in a NPP by analyzing the air velocity and temperature distribution. Understanding the air-flow distribution within the MCR is critical to maintaining a habitable environment, particularly under accident conditions. In this study, we analyzed the air-flow velocity and temperature distribution in the habitable-area of the MCR under Case 1 working conditions for a 24 hours period. As shown in fig. 10, the personnel activity area had air-flow velocities ranging from 0 to 0.9 m/s. The high speed jet from the air supply outlet resulted in localized areas of higher air-flow velocity, while most indoor areas had air-flow velocities lower than 0.2 m/s.

Indoor air velocity and temperature distribution near personnel

The cross-sectional positions in figs. 9(a)-9(c) are analyzed to understand the impact of air supply air-flow and thermal convection of human heat sources on the air-flow distribution. The cross-section in fig. 10(a) is located at the rear side of the air supply opening and is

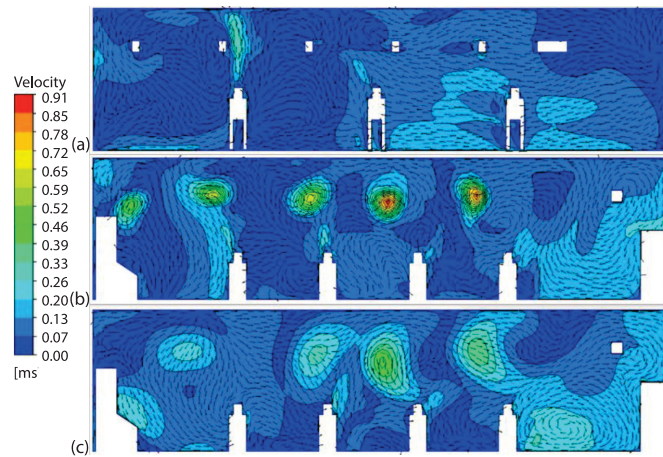


Figure 9. Velocity distribution of vertical section; (a) P1, (b) P2, and (c) P3

not influenced by the air supply air-flow. However, the thermal convection generated by human heat sources generates a buoyancy force, causing the air-flow to mainly move upward. The cross-section in fig. 9(b) is more affected by the air supply jet. The velocity of the area affected by the air supply jet is significantly higher than the surrounding air-flow velocity, with a maximum of 0.9 m/s. For the cross-section in fig. 9(c), the impact of the air supply jet is greatly reduced, with a maximum air-flow velocity of 0.45 m/s. This is because the air-flow ejected from the air supply outlet expands and moves forward, and as the distance increases, there is a lack of inertial force to continue to maintain the horizontal expansion of the air-flow, resulting in a smaller air-flow velocity. Moreover, higher air-flow velocities near the wall can be observed in all three cross-sectional profiles.

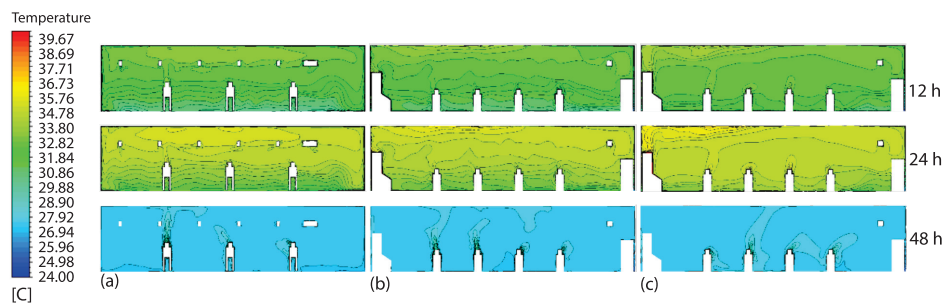


Figure 10. Temperature distribution in the vertical section of the personnel residence area at different times; (a) P1, (b) P2, and (c) P3

Based on the data presented in fig. 8, it can be observed that the indoor air temperature exhibited an increasing trend from 0-24 hours, reaching its highest point at 24 hours. Subsequently, the temperature gradually decreased from 24-72 hours, and eventually stabilized after 48 hours. Three time points were selected for analysis, namely 12 hours, 24 hours, and 48 hours, with ambient temperatures of 32.65 °C, 34.62 °C, and 27.61 °C, respectively. Furthermore, information on the temperature distribution in the vicinity of the individuals at these three time points is provided below.

Figures 10(a)-10(c) depict the temperature distribution at three rows of personnel (P1, P2, and P3) at 12 hours, 24 hours, and 48 hours, respectively. The results indicate that the ambient temperature near the personnel in the MCR increased from 31.8-33.8 °C during the 12 hours and 24 hours measurements, which met the requirements for personnel habitability. And at 48 hours, the temperature near the personnel dropped to 27.5 °C.

Furthermore, the indoor air temperature was found to be highest at 24 hours. As the right side of the room had fewer equipment and was located further away from heat sources, the temperature near the right wall was the lowest. In contrast, the left wall had more heat source devices, resulting in a higher temperature compared to the right wall. The air-flow in the room was influenced by the heat sources and circulated roughly in a clockwise direction. The air-flow on the left side of the room was influenced by thermal convection, resulting in an upward movement of air. Once it reached the ceiling, the air moved horizontally towards the right wall, and finally, returned along the floor, as shown in fig. 11.

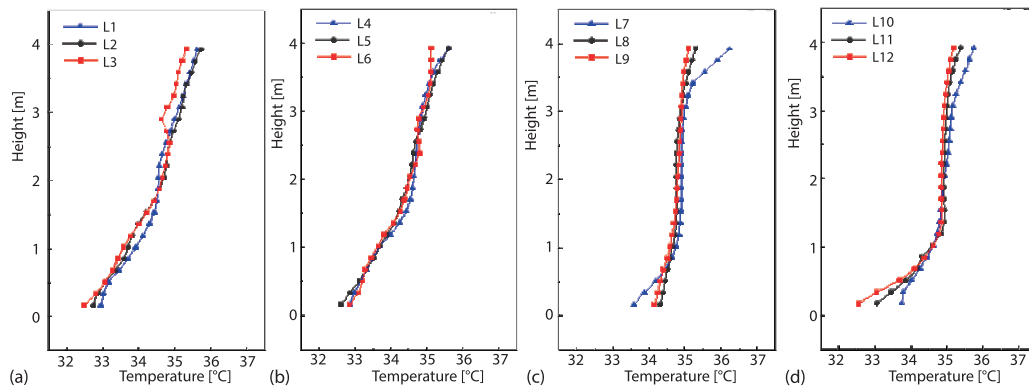


Figure 11. Temperature profiles along the height direction

Figure 2 displays the location of measurement points, which are concentrated in the main activity area of personnel. Meanwhile, fig. 11 illustrates the trend of air temperature with height at various locations in the MCR. It can be observed that the temperature near the ceiling is the highest, with a temperature of approximately 35.5 °C. This phenomenon is attributed to the upward movement of hot air due to buoyancy force, which concentrates on the ceiling and raises the temperature. Additionally, the temperature on the left side of the MCR is higher than other locations at the same height, such as L7 and L10, because more heat is dissipated from the equipment on the left side, leading to a higher temperature.

Figure 11(a) indicates that line 1 records the highest temperature of 35.6 °C at the height position of 3.9 m, demonstrating clear temperature stratification in the cross-section. This phenomenon is caused by lower hot air density, which leads to hot air-driven flow and results in a higher temperature in the upper part. The velocity vector diagram in fig. 10 shows that the hot air in the lower part rises upward due to the buoyancy force, supporting the use of the Boussinesq approximation. The temperature distribution in fig. 11(b) resembles that in fig. 11(a), with a visible temperature stratification at this location, where the upper air temperature is higher than the lower air temperature. The vertical temperature rise is 2.7 °C, with a vertical temperature rise rate of 0.72 °C per hour. In contrast, fig. 11(c) shows that the indoor temperature distribution at this section is relatively uniform, with no stratification. This is due to the equipment's heat dissipation affecting the lower air temperature, resulting in a small difference between the upper and lower air temperatures. Figure 11(d) displays the temperature trend at

L10-L12, which is located farther from the air supply and less affected by the jet disturbance. The temperature at L10 is higher than that at L11 and L12, reaching a maximum of 35.75 °C.

Figure 12 presents the distribution of the air-flow field in the MCR, revealing sudden velocity change points influenced by the air supply jet. The mutation point on L6 records the highest velocity of 0.66 m/s due to the air supply jet passing through L6 location. The jet's movement is propelled forward by the inertial force, which gradually decreases with distance. As a result, the highest velocity point's height decreases from 2.9 m in fig. 12(b) to nearly 2 m in fig. 12(d).

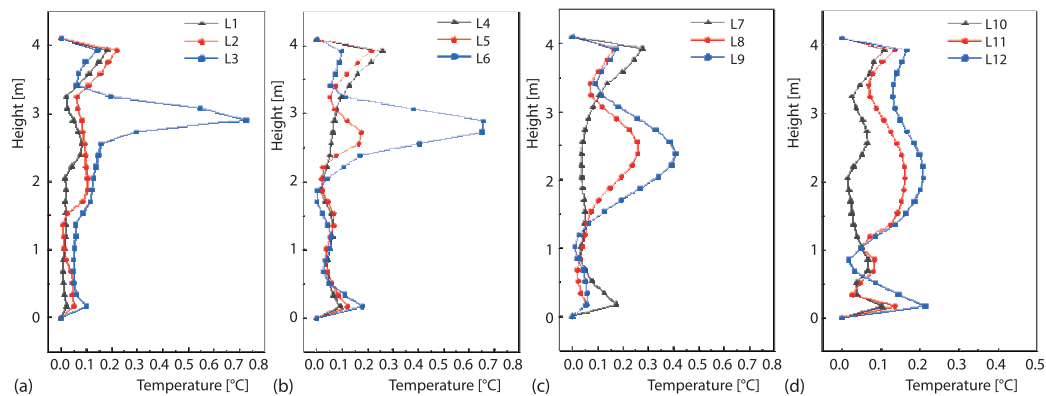


Figure 12. Velocity profile along the height direction

Figures 12(a)-12(c) are significantly affected by the air supply jet, resulting in large local forced convection. However, the personnel activity area is primarily concentrated below 2 m. There are no sudden velocity change points in the area below 2 m, and the air-flow distribution is relatively uniform. Consequently, the air supply jet has little impact on personnel. The average wind speed calculated in the area below 2 m, excluding the near-wall, is 0.07 m/s. The perceived wind strength is not very strong, meeting the requirements of the *Design Code for Heating, Ventilation and Air Conditioning in Civil Buildings*.

The CO₂ concentration field

The concentration of CO₂ in a room is primarily influenced by the number of occupants (individuals or residents within a building) and their metabolic activity. In the control room, the number of occupants is fixed at 11 people, therefore, the CO₂ concentration is mainly determined by human metabolism. Figure 13 shows that the indoor CO₂ concentration trends are similar in Cases 1 and 3, but the CO₂ concentration in Case 3 is lower than in Case 1. In both cases, the average CO₂ concentration in the control room exceeds 800 ppm after 3.5 hours and reaches over 1000 ppm after 6 hours. Subsequently, the CO₂ concentration continues to rise and stabilizes gradually after 30 hours. In Case 1, the average CO₂ concentration stabilizes between 1560 ppm and 1590 ppm, while in Case 3, the average CO₂ concentration stabilizes be-

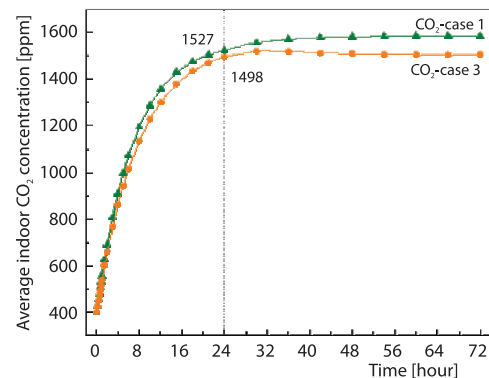


Figure 13. Temporal variations in average indoor CO₂ concentration

tween 1500 ppm and 1530 ppm. Therefore, the average CO₂ concentration in Case 1 is 70 ppm higher than in Case 3.

Figure 14 presents contour plots of the CO₂ concentration under two cases, revealing the uneven distribution of indoor CO₂ concentration over a 24 hours period. In Case 1, the difference between the minimum and maximum CO₂ concentrations is about 29 ppm, with a minimum concentration of 1515 ppm and a maximum concentration of 1544 ppm. The CO₂ concentration on the left side is lower than on the right side, which may be due to the limited supply of fresh air, leading to a CO₂ peak in the middle of the first row of occupants. In Case 3, the difference between the minimum and maximum CO₂ concentrations is also about 29 ppm, with a minimum concentration of 1486 ppm and a maximum concentration of 1516 ppm. The CO₂ concentration on the left side is higher than on the right side, which may be due to the occupants gathering together, resulting in a relatively lower CO₂ concentration in front of the control room. Despite the maximum level of CO₂ exhaled by the occupants being set, the results indicate that the CO₂ concentrations in all areas meet the requirements for habitability.

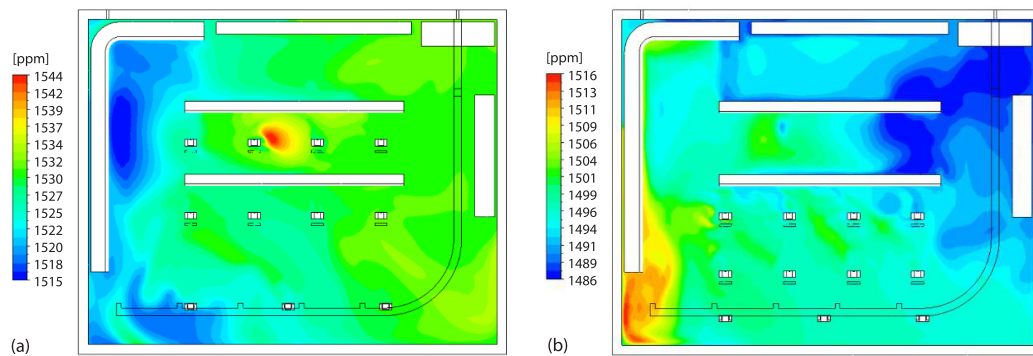


Figure 14. Contours of the CO₂ concentration (ppm) on the horizontal plan $z = 1$ m; (a) Case1 and (b) Case 3

The impact of personnel position

Based on the comparison of the two working conditions in fig. 8, it can be observed that there is little difference in the indoor temperature change trend, with a nearly constant temperature at each time point. However, the first row of personnel in case1 was found to be located in a relatively high temperature area, as shown in fig. 2. To improve the indoor thermal comfort, the position of personnel was optimized by moving the first row of personnel to the back of the relatively low temperature area. The impact of the optimized personnel station on the indoor thermal environment was investigated by comparing the habitable-area before and after the change. Significant changes in the average temperature and velocity were observed, as shown in figs. 15(a) and 15(b), respectively.

Figure 15(a) presents the average temperature variation in the space below 2.2 m in the main personnel activity area for both Case 1 and Case 3, before and after the personnel station optimization. The results showed that the indoor temperature increases with height in both cases. However, after optimizing the personnel station, the average temperature of the personnel activity area decreased by 0.42 °C compared to Case 1. This improvement can be attributed to the better distribution of the heat sources after moving the first row of personnel to a relatively cooler area.

Furthermore, fig. 15(b) shows the comparison of the average velocity before and after the optimized personnel station. It can be observed that the average velocity in both Case 1 and Case 3 was maintained below 0.2 m/s, and the average velocity in Case 3 was lower than that in Case 1. This can be attributed to the weakened influence of the air supply jet after the personnel moved to the back row, resulting in lower wind speeds. The optimized personnel station not only improves the thermal comfort of the indoor environment but also reduces the air velocity in the personnel activity area, which is beneficial for meeting the requirements of habitability.

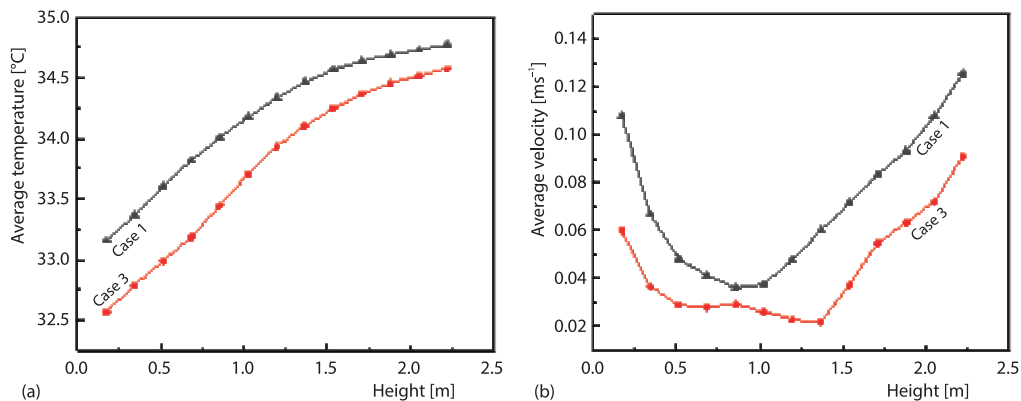


Figure 15. Comparison of average temperature and average speed of habitable-area in two cases

This study conducted an in-depth investigation into the influence of the average CO₂ concentration in the habitable-area with height change under two working conditions fig. 16 shows that the average CO₂ concentration in the habitable-area under Case 1 is higher than that under Case 3, with a difference of 30 ppm on average. This indicates that the location of personnel has a certain impact on the distribution of indoor CO₂ concentration. Additionally, this study found that indoor CO₂ concentration gradually increases with height, which is most evident under Case 3. The CO₂ concentration below 1 m is 1495 ppm, and it starts to increase above 1 m, reaching 1530 ppm at 2 m, an increase of 35 ppm. The reason for this phenomenon is that under Case 3, people are concentrated in certain locations, and CO₂ exhaled and moves upward with the hot air, leading to a higher concentration of CO₂ at higher locations. In contrast, in Case 1, due to the dispersion of personnel, the CO₂ concentration varies more uniformly with height. Additionally, this study found that under both working conditions, the CO₂ concentration in all areas is below the habitable requirements, indicating that the current ventilation system has a good effect on maintaining indoor air quality. This result provides an important reference for the design and optimization of indoor environments.

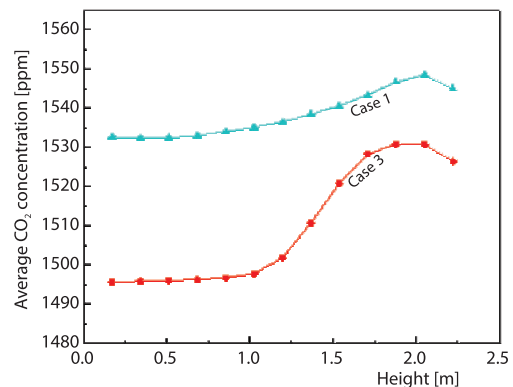


Figure 16. Comparison of average CO₂ concentration of habitable-area in two cases

Conclusions

In this paper, the air-flow organization in the MCR of a NPP was studied by numerical simulation using CFD method, as well as the thermal conduction characteristic of the MCR enclosure under unsteady conditions. The simulation results show that.

- The control room walls play a crucial role in reducing indoor air temperature during the entire power outage scenario in the NPP. Without these walls, the indoor temperature would rapidly increase within a short period, surpassing the maximum allowable temperature for habitability requirements, thus failing to meet the habitability standards indoors.
- The heat storage capacity and fresh air supply of the MCR enclosure structure can meet the habitability requirements of the MCR under certain conditions. For example, in Case 1, the temperature rise in the MCR over 24 hours is 11.62 °C, resulting in an indoor environment temperature of approximately 34.62 °C, which meets habitability requirements.
- The thermal storage analysis of the walls indicates that the thermal storage performance is influenced by the heat flux density, with the temperature rise rate of walls in high heat flux density areas greater than those in low heat flux density areas. Therefore, the temperature rise rates of walls S1 and S4, located near the heat-generating equipment, are higher than those of walls S2 and S3. In particular, internal heat transfer analysis of wall S2 reveals that the temperature rise rates at $d = 0$ m, $d = 0.13$ m, and $d = 0.4$ m are 0.215, 0.133, and 0.077, respectively. This indicates that the influence of internal heat flux on the wall decreases gradually with increasing depth.
- Analysis of the temperature and velocity fields near the indoor personnel reveals higher temperatures near the heat sources, potentially causing discomfort to individuals. Therefore, optimizations were made to the positioning of personnel. Following optimization, the temperature in the personnel activity area decreased by 0.42 °C, and the average indoor CO₂ concentration decreased by 30 ppm. Consequently, optimization adjustments can be made to the working area of personnel in the control room. The findings of this study provide valuable insights for the design and optimization of indoor environments in similar scenarios.

Nomenclature

d – hydraulic diameter, [m]
 I – turbulence intensity, [%]
 k – thermal conductivity, [Wm⁻¹K⁻¹]
 Re – Reynolds number ($=vd/\mu$), [-]
 T – temperature, [°C]
 \vec{v} – fluid velocity vector, [ms⁻¹]
 z – vertical co-ordinate, [m]

Greek symbols

ε – turbulence dissipation, [m²s⁻³]
 μ – dynamic viscosity, [kgm⁻¹s⁻¹]

Acronyms

NPP – nuclear power plant
 MCR – main control room

References

- [1] Liu, P., et al., Accommodation Issue of Nuclear Power in China: Status Quo, Barriers and Solutions, *Energy Strategy Rev.*, 22 (2018), Nov., pp. 166-178
- [2] Chang, Y.-C., Zhao, Y., The Fukushima Nuclear Power Station Incident and Marine Pollution, *Mar. Pollut. Bull.*, 64 (2012), 5, pp. 897-901
- [3] Hollnagel, E., The Fukushima Disaster – Systemic Failures as the Lack of Resilience, *Nucl. Eng. Technol.*, 45 (2013), 1, pp. 13-20
- [4] Orosa, J. A., Oliveira, A. C., A Field Study on Building Inertia and Its Effects on Indoor Thermal Environment, *Renew. Energy*, 37 (2012), 1, pp. 89-96
- [5] ***, International Nuclear Safety Advisory Group and International Atomic Energy Agency, Eds., Basic safety principles for nuclear power plants: 75-INSAG-3 Rev. 1, Rev. Vienna: International Atomic Energy Agency, 1999

- [6] Zheng, G., Zhao X., Optimization of the Main Control Room Habitability System in Nuclear Power Plant (in Chinese), *China Nuclear Power*, 6 (2013), 4, pp. 291-295
- [7] Zhang, G., Wang, C., Emergency Habitability System for Main Control Room of AP1000 Third Generation Nuclear Power Plant (in Chinese), *HV&AC*, 47 (2017), pp. 32-35
- [8] Li, H., *et al.*, Study on the Passive Refrigeration for Main Control Room of Nuclear Power Plant in Power Outage Accident, *Nucl. Eng. Des.*, 326 (2018), Jan., pp. 183-189
- [9] Zheng, S., Xu, N., The Study on the Test of the Track of the Dynamic Cooling Load of the DVC System (in Chinese), *Energy Conservation Technology*, 28 (2010), pp. 424-426
- [10] Abed, F. M., *et al.*, Effect of Climate and Design Parameters on the Temperature Distribution of a Room, *Jou. Build. Eng.*, 17 (2018), May, pp. 115-124
- [11] ***, NBT 20395-2017-Residential Design Requirements for the Control Room.pdf., <https://max.book118.com/html/2019/0613/7060054031002033.shtm>, 2022
- [12] Wouters, P., *et al.*, Ventilation Requirements in non-Domestic Buildings and Energy Efficiency, *Energy and Buildings*, 27 (1988), 3, pp. 257-261
- [13] Schulz, T. L., Westinghouse AP1000 Advanced Passive Plant, *Nucl. Eng. Des.*, 236 (2006), 14-16, pp. 1547-1557
- [14] Jia, Y., *et al.*, Refrigerating Characteristics of Ice Storage Capsule for Temperature Control of Coal Mine Refuge Chamber, *Appl. Therm. Eng.*, 75 (2015), Jan., pp. 756-762
- [15] Wang, S., *et al.*, A New Compressed Air Energy Storage Refrigeration System, *Energy Convers. Manag.*, 47 (2006), 18-19, pp. 3408-3416
- [16] Siddiqui, F. R., *et al.*, Exergo-Economic Analysis of a Solar Driven Hybrid Storage Absorption Refrigeration Cycle, *Energy Convers. Manag.*, 80 (2014), Apr., pp. 165-172
- [17] Sutharshan, B., *et al.*, The AP1000TM Reactor: Passive Safety and Modular Design, *Energy Procedia*, 7 (2011), Dec., pp. 293-302
- [18] Huang, Y., *et al.*, Dynamic Thermal Performance Analysis for Fin-Concrete Ceiling in Main Control Rooms of Passive Nuclear Power Plants, *Case Stud. Therm. Eng.*, 28 (2021), 101402
- [19] Al-Rukaibawi, L. S., *et al.*, Numerical Simulation of the Effect of Bamboo Composite Building Envelope on Summer Overheating Problem, *Case Stud. Therm. Eng.*, 28 (2021), 101516
- [20] Gollapudi, L. N., *et al.*, Numerical Heat Transfer Analysis of a Thermal Energy Storage System Enclosure with Horizontal Fin for Sustainable Energy Storage, *Case Stud. Therm. Eng.*, 28 (2021), 101670
- [21] Palanisamy, D., Ayalur, B. K., Development and Testing of Condensate Assisted pre-Cooling Unit for Improved Indoor Air Quality in a Computer Laboratory, *Build. Environ.*, 163 (2019), 106321